

# Broadband terahertz conductivity and optical transmission of indium-tin-oxide (ITO) nanomaterials

Chan-Shan Yang,<sup>1</sup> Chan-Ming Chang,<sup>1</sup> Po-Han Chen,<sup>2</sup> Peichen Yu,<sup>2</sup> and Ci-Ling Pan<sup>1,3,\*</sup>

<sup>1</sup>Department of Physics, National Tsing Hua University, Hsinchu, 30013, Taiwan

<sup>2</sup>Department of Photonics and Institute of Electro-Optical Engineering, National Chiao Tung University, Hsinchu, 30010, Taiwan

<sup>3</sup>Frontier Research Center on Fundamental and Applied Science of Matters, Hsinchu, 30013, Taiwan  
\*clpan@phys.nthu.edu.tw

**Abstract:** Indium-tin-oxide (ITO) nanorods (NRs) and nanowhiskers (NWs) were fabricated by an electron-beam glancing-angle deposition (GLAD) system. These nanomaterials are of interests as transparent conducting electrodes in various devices. Two terahertz (THz) time-domain spectrometers (TDS) with combined spectral coverage from 0.15 to 9.00 THz were used. These allow accurate determination of the optical and electrical properties of such ITO nanomaterials in the frequency range from 0.20 to 4.00 THz. Together with Fourier transform infrared spectroscopic (FTIR) measurements, we found that the THz and far-infrared transmittance of these nanomaterials can be as high as 70% up to 15 THz, as opposed to about 9% for sputtered ITO thin films. The complex conductivities of ITO NRs, NWs as well films are well fitted by the Drude-Smith model. Taking into account that the volume filling factors of both type of nanomaterials are nearly same, mobilities, and DC conductivities of ITO NWs are higher than those of NRs due to less severe carrier localization effects in the former. On the other hand, mobilities of sputtered ITO thin films are poorer than ITO nanomaterials because of larger concentration of dopant ions in films, which causes stronger carrier scattering. We note further that consideration of the extreme values of  $\text{Re}\{\sigma\}$  and  $\text{Im}\{\sigma\}$  as well the inflection points, which are functions of the carrier scattering time ( $\tau$ ) and the expectation value of cosine of the scattering angle ( $\gamma$ ), provide additional criteria for accessing the accuracy of the extraction of electrical parameters of non-Drude-like materials using THz-TDS. Our studies so far indicate ITO NWs with heights of  $\sim 1000$  nm show outstanding transmittance and good electrical characteristics for applications such as transparent conducting electrodes of THz Devices.

©2013 Optical Society of America

**OCIS codes:** (040.2235) Far infrared or terahertz; (120.4290) Nondestructive testing; (120.4530) Optical constants; (160.4236) Nanomaterials; (220.4241) Nanostructure fabrication; (260.2065) Effective medium theory; (290.1350) Backscattering; (300.6270) Spectroscopy, far infrared; (300.6495) Spectroscopy, terahertz; (350.5400) Plasmas.

---

## References and links

1. J. W. Shim, H. Cheun, J. Meyer, C. Fuentes-Hernandez, A. Dindar, Y. H. Zhou, D. K. Hwang, A. Kahn, and B. Kippelen, "Polyvinylpyrrolidone-modified indium tin oxide as an electron-collecting electrode for inverted polymer solar cells," *Appl. Phys. Lett.* **101**(7), 073303 (2012).
2. Ö. Şenlik, H. Y. Cheong, and T. Yoshie, "Design of subwavelength-size, indium tin oxide (ITO)-clad optical disk cavities with quality-factors exceeding  $10^4$ ," *Opt. Express* **19**(23), 23469–23474 (2011).

3. Y.-J. Liu, C.-C. Huang, T.-Y. Chen, C.-S. Hsu, J.-K. Liou, T.-Y. Tsai, and W.-C. Liu, "Implementation of an indium-tin-oxide (ITO) direct-Ohmic contact structure on a GaN-based light emitting diode," *Opt. Express* **19**(15), 14662–14670 (2011).
4. S.-Y. Liu, Y.-C. Lin, J.-C. Ye, S. J. Tu, F. W. Huang, M. L. Lee, W. C. Lai, and J. K. Sheu, "Hydrogen gas generation using n-GaN photoelectrodes with immersed Indium Tin oxide Ohmic contacts," *Opt. Express* **19**(S6 Suppl 6), A1196–A1201 (2011).
5. C. K. Choi, K. D. Kihm, and A. E. English, "Optoelectric biosensor using indium-tin-oxide electrodes," *Opt. Lett.* **32**(11), 1405–1407 (2007).
6. P. Yu, C.-H. Chang, C.-H. Chiu, C.-S. Yang, J.-C. Yu, H.-C. Kuo, S.-H. Hsu, and Y.-C. Chang, "Efficiency enhancement of GaAs photovoltaics employing antireflective indium tin oxide nanocolumns," *Adv. Mater.* **21**(16), 1618–1621 (2009).
7. P. Yu, C.-H. Chang, M.-S. Su, M.-H. Hsu, and K.-H. Wei, "Embedded indium-tin-oxide nanoelectrodes for efficiency and lifetime enhancement of polymer-based solar cells," *Appl. Phys. Lett.* **96**(15), 153307 (2010).
8. J. W. Leem and J. S. Yu, "Glancing angle deposited ITO films for efficiency enhancement of a-Si:H/ $\mu$ c-Si:H tandem thin film solar cells," *Opt. Express* **19**(S3 Suppl 3), A258–A268 (2011).
9. C.-H. Chang, M.-H. Hsu, P.-C. Tseng, P. Yu, W.-L. Chang, W.-C. Sun, and W.-C. Hsu, "Enhanced angular characteristics of indium tin oxide nanowhisker-coated silicon solar cells," *Opt. Express* **19**(S3 Suppl 3), A219–A224 (2011).
10. D.-J. Seo, J.-P. Shim, S.-B. Choi, T. H. Seo, E.-K. Suh, and D.-S. Lee, "Efficiency improvement in InGaN-based solar cells by indium tin oxide nano dots covered with ITO films," *Opt. Express* **20**(S6), A991–A996 (2012).
11. J. W. Leem and J. S. Yu, "Indium tin oxide subwavelength nanostructures with surface antireflection and superhydrophilicity for high-efficiency Si-based thin film solar cells," *Opt. Express* **20**(S3), A431–A440 (2012).
12. C.-H. Chang, P. Yu, M.-H. Hsu, P.-C. Tseng, W.-L. Chang, W.-C. Sun, W.-C. Hsu, S.-H. Hsu, and Y.-C. Chang, "Combined micro- and nano-scale surface textures for enhanced near-infrared light harvesting in silicon photovoltaics," *Nanotechnology* **22**(9), 095201 (2011).
13. C. H. Chiu, P. Yu, C. H. Chang, C. S. Yang, M. H. Hsu, H. C. Kuo, and M. A. Tsai, "Oblique electron-beam evaporation of distinctive indium-tin-oxide nanorods for enhanced light extraction from InGaN/GaN light emitting diodes," *Opt. Express* **17**(23), 21250–21256 (2009).
14. T. H. Seo, K. J. Lee, A. H. Park, C.-H. Hong, E.-K. Suh, S. J. Chae, Y. H. Lee, T. V. Cuong, V. H. Pham, J. S. Chung, E. J. Kim, and S.-R. Jeon, "Enhanced light output power of near UV light emitting diodes with graphene / indium tin oxide nanodot nodes for transparent and current spreading electrode," *Opt. Express* **19**(23), 23111–23117 (2011).
15. Y. Y. Kee, S. S. Tan, T. K. Yong, C. H. Nee, S. S. Yap, T. Y. Tou, G. Sáfrán, Z. E. Horváth, J. P. Moscatello, and Y. K. Yap, "Low-temperature synthesis of indium tin oxide nanowires as the transparent electrodes for organic light emitting devices," *Nanotechnology* **23**(2), 025706 (2012).
16. S. H. Lee and N. Y. Ha, "Nanostructured indium-tin-oxide films fabricated by all-solution processing for functional transparent electrodes," *Opt. Express* **19**(22), 21803–21808 (2011).
17. C.-S. Yang, M.-H. Lin, C.-H. Chang, P. Yu, J.-M. Shieh, C.-H. Shen, O. Wada, and C.-L. Pan, "Non-Drude behavior in indium-tin-oxide nanowhiskers and thin films by transmission and reflection THz time-domain spectroscopy," *IEEE J. Quantum Electron.*, accepted (2013).
18. T. Bauer, J. S. Kolb, T. Löffler, E. Mohler, U. C. Pernisz, and H. G. Roskos, "Indium-tin-oxide-coated glass as dichroic mirror for far-infrared electromagnetic radiation," *J. Appl. Phys.* **92**(4), 2210–2212 (2002).
19. J. Kröll, J. Darmo, and K. Unterrainer, "Metallic wave-impedance matching layers for broadband terahertz optical systems," *Opt. Express* **15**(11), 6552–6560 (2007).
20. S. A. Jewell, E. Hendry, T. H. Isaac, and J. R. Sambles, "Tuneable Fabry-Perot etalon for terahertz radiation," *New J. Phys.* **10**(3), 033012 (2008).
21. D. G. Cooke and P. U. Jepsen, "Optical modulation of terahertz pulses in a parallel plate waveguide," *Opt. Express* **16**(19), 15123–15129 (2008).
22. C. H. Chang, P. Yu, and C. S. Yang, "Broadband and omnidirectional antireflection from conductive indium-tin-oxide nanocolumns prepared by glancing-angle deposition with nitrogen," *Appl. Phys. Lett.* **94**(5), 051114 (2009).
23. I. Hamberg, A. Hjortsberg, and C. G. Granqvist, "High quality transparent heat reflectors of reactively evaporated indium tin oxide," *Appl. Phys. Lett.* **40**(5), 362–364 (1982).
24. Q. Wan, Z. T. Song, S. L. Feng, and T. H. Wang, "Single-crystalline tin-doped indium oxide whiskers: synthesis and characterization," *Appl. Phys. Lett.* **85**(20), 4759–4761 (2004).
25. S.-P. Chiu, H.-F. Chung, Y.-H. Lin, J.-J. Kai, F.-R. Chen, and J.-J. Lin, "Four-probe electrical-transport measurements on single indium tin oxide nanowires between 1.5 and 300 K," *Nanotechnology* **20**(10), 105203 (2009).
26. J. Gao, R. Chen, D. H. Li, L. Jiang, J. C. Ye, X. C. Ma, X. D. Chen, Q. H. Xiong, H. D. Sun, and T. Wu, "UV light emitting transparent conducting tin-doped indium oxide (ITO) nanowires," *Nanotechnology* **22**(19), 195706 (2011).
27. C.-S. Yang, C.-H. Chang, M.-H. Lin, P. Yu, O. Wada, and C.-L. Pan, "THz conductivities of indium-tin-oxide nanowhiskers as a graded-refractive-index structure," *Opt. Express* **20**(S4 Suppl 4), A441–A451 (2012).

28. C.-W. Chen, Y.-C. Lin, C.-H. Chang, P. Yu, J.-M. Shieh, and C.-L. Pan, "Frequency-dependent complex conductivities and electric responses of indium tin oxide thin films from the visible to the far-infrared," *IEEE J. Quantum Electron.* **46**(12), 1746–1754 (2010).
29. G. M. Turner, M. C. Beard, and C. A. Schmuttenmaer, "Carrier localization and cooling in dye-sensitized nanocrystalline titanium dioxide," *J. Phys. Chem. B* **106**(45), 11716–11719 (2002).
30. H. Němec, P. Kužel, and V. Sundström, "Far-infrared response of free charge carriers localized in semiconductor nanoparticles," *Phys. Rev. B* **79**(11), 115309 (2009).
31. J. B. Baxter and C. A. Schmuttenmaer, "Conductivity of ZnO nanowires, nanoparticles, and thin films using time-resolved terahertz spectroscopy," *J. Phys. Chem. B* **110**(50), 25229–25239 (2006).
32. G. Ma, D. Li, H. Ma, J. Shen, C. Wu, J. Ge, S. Hu, and N. Dai, "Carrier concentration dependence of terahertz transmission on conducting ZnO films," *Appl. Phys. Lett.* **93**(21), 211101 (2008).
33. X. Zou, J. Luo, D. Lee, C. Cheng, D. Springer, S. K. Nair, S. A. Cheong, H. J. Fan, and E. E. M. Chia, "Temperature-dependent terahertz conductivity of tin oxide nanowire films," *J. Phys. D Appl. Phys.* **45**(46), 465101 (2012).
34. D. Tsokkou, A. Othonos, and M. Zervos, "Carrier dynamics and conductivity of SnO<sub>2</sub> nanowires investigated by time-resolved terahertz spectroscopy," *Appl. Phys. Lett.* **100**(13), 133101 (2012).
35. I.-C. Ho, X. Guo, and X.-C. Zhang, "Design and performance of reflective terahertz air-biased-coherent-detection for time-domain spectroscopy," *Opt. Express* **18**(3), 2872–2883 (2010).
36. B. Clough, J. Liu, and X.-C. Zhang, "All air-plasma" terahertz spectroscopy," *Opt. Lett.* **36**(13), 2399–2401 (2011).
37. N. Vieweg, B. M. Fischer, M. Reuter, P. Kula, R. Dabrowski, M. A. Celik, G. Frenking, M. Koch, and P. U. Jepsen, "Ultrabroadband terahertz spectroscopy of a liquid crystal," *Opt. Express* **20**(27), 28249–28256 (2012).
38. G. Gallot and D. Grischkowsky, "Electro-optic detection of terahertz radiation," *J. Opt. Soc. Am. B* **16**(8), 1204–1212 (1999).
39. C.-L. Pan, C.-F. Hsieh, R.-P. Pan, M. Tanaka, F. Miyamaru, M. Tani, and M. Hangyo, "Control of enhanced THz transmission through metallic hole arrays using nematic liquid crystal," *Opt. Express* **13**(11), 3921–3930 (2005).
40. C.-S. Yang, C.-J. Lin, R.-P. Pan, C. T. Que, K. Yamamoto, M. Tani, and C.-L. Pan, "The complex refractive indices of the liquid crystal mixture E7 in the terahertz frequency range," *J. Opt. Soc. Am. B* **27**(9), 1866–1873 (2010).
41. C.-K. Lee, C.-S. Yang, S.-H. Lin, S.-H. Huang, O. Wada, and C.-L. Pan, "Effects of two-photon absorption on terahertz radiation generated by femtosecond-laser excited photoconductive antennas," *Opt. Express* **19**(24), 23689–23697 (2011).
42. N. V. Smith, "Classical generalization of the Drude formula for the optical conductivity," *Phys. Rev. B* **64**(15), 155106 (2001).
43. L. V. Titova, T. L. Cocker, D. G. Cooke, X. Wang, A. Meldrum, and F. A. Hegmann, "Ultrafast percolative transport dynamics in silicon nanocrystal films," *Phys. Rev. B* **83**(8), 085403 (2011).
44. J. Ederth, "Electrical transport in nanoparticle thin films of gold and indium tin oxide," Ph.D. dissertation, Dept. Mat. Science, Uppsala Univ., Uppsala, Sweden, (2003).
45. H.-K. Nienhuys and V. Sundström, "Influence of plasmons on terahertz conductivity measurements," *Appl. Phys. Lett.* **87**(1), 02101 (2005).
46. P. Parkinson, L.-H. James, Q. Gao, H. H. Tan, C. Jagadish, M. B. Johnston, and L. M. Herz, "Transient terahertz conductivity of GaAs nanowires," *Nano Lett.* **7**(7), 2162–2165 (2007).

## 1. Introduction

Indium-tin-oxide (ITO), one kind of heavily-doped transparent conductive oxides (TCOs), has been widely employed as transparent conducting electrode and direct-Ohmic contact layers in optoelectronic devices, due to its high transmittance and low resistivity in the visible [1–5]. More recently, ITO nanomaterials, e.g. nanocolumn, nanorods (NRs), nanowires, nanodots, and nanowhiskers (NWs), are reported to have the omnidirectional, broadband anti-reflective (AR) characteristics, and superhydrophilicity for improving the function of solar cells [6–12], light emitting diodes (LEDs) [13, 14], organic LEDs [15], and displays [16]. Further, the ITO NWs were found to exhibit superb terahertz (THz) transparency, mobility, and comparable conductivities to sputtered thin films [17]. Previously, ITO thin films were employed in optoelectronic devices for manipulation of the THz radiation [18–21]. Unfortunately, because of the issue of high plasma frequencies (several hundred THz), the sputtered ITO thin film exhibits high reflectance in the infrared and THz region [17, 22]. Therefore, ITO nanomaterials mentioned previously are interesting alternatives as transparent electrodes for THz devices. Several studies have reported the (visible) optical [6, 9, 12, 13, 23], and electrical properties of ITO nanomaterials [24–26]. However, the conventional

methods of characterizing electrical properties of materials can damage the morphology of nanomaterials because of the need of electrical contacts, or just provide information on the mobility and resistivity of an individual nanostructure [24–26].

Terahertz time-domain spectroscopy (THz-TDS), as a non-destructive method of probing the optical and microscopic electrical properties, has been extensively employed to study several bulk and nanomaterials of TCOs, e.g., ITO [17, 27, 28], titanium dioxide ( $\text{TiO}_2$ ) [29, 30], zinc oxide ( $\text{ZnO}$ ) [30–32], and tin oxide ( $\text{SnO}_2$ ) [33, 34]. In our previous study, we have reported the frequency-dependent complex conductivities ( $\sigma^* = \text{Re}\{\sigma\} + i \text{Im}\{\sigma\}$ ), which were described by Drude model, of certain sputtered ITO thin films with thickness in the range of 189–962 nm [28]. Also, carrier localization in the bottom layer atop the substrate of ITO NWs, for which the electrical properties were found to be fit well by the Drude-Smith model, was reported by our group [27]. By applying the transmission-type and reflection-type THz-TDS, and X-Ray diffraction, our group has also clarified the mechanism of carrier localization in the ITO thin films and NWs [17]. Unfortunately, these data are limited to frequencies below approximately 2.0 THz. At these low frequencies, features of  $\sigma^*$ , specifically the maximum and minimum of  $\text{Re}\{\sigma\}$  and  $\text{Im}\{\sigma\}$ , and the angular frequency at which  $\text{Im}\{\sigma\}$  crosses zero, cannot be nearly observed. Therefore, the description of non-Drude behavior of ITO nanomaterials is not complete and accurate enough, as shown in this work. Besides, for the electrical properties of ITO NWs, the role of branches which grow perpendicularly to the trunk has not been well understood.

Recently, broadband THz emission systems based on a gaseous plasma with incommensurate dual-color ( $\omega$ - $2\omega$ ) excitation has been demonstrated [35–37]. Such systems have known been increasingly used in the THz-TDS system to study materials, e.g., nonlinear crystals [35], explosives [36], and liquid crystals [37], with features at frequencies above 2 THz. However, the signal-to-noise ratio (SNR) of this approach is often inferior to that of the photoconductive (PC) antenna-based THz-TDS in the frequency range below the 0.5 THz [35–37].

In this paper, ITO nanomaterials (NRs and NWs), were prepared by an electron-beam glancing-angle deposition (GLAD) system [13]. Two terahertz (THz) time-domain spectrometers (TDS) based respectively on dual-color laser-induced gaseous plasma and photoconductive (PC) antenna were applied to study the optical and electrical properties of such ITO nanomaterials in the frequency range from 0.20 to 4.00 THz. Together with Fourier transform infrared spectroscopic (FTIR) measurements, we determined both the THz and far-infrared transmittance of these nanomaterials. The complex conductivities of ITO NRs, NWs as well as films are determined by fitting with the Drude-Smith model. Taking into account that the volume filling factors of both type of nanomaterials, mobilities and DC conductivities of ITO NWs and NRs were retrieved to ascertain mechanisms of carrier localization. Finally, we show that new features of complex conductivities in non-Drude-like materials from relatively broadband THz measurements reported in this work.

## 2. Experimental methods

### 2.1. Sample preparation and characterization

In the electron-beam GLAD system, the target source placed on the bottom center of the chamber consisted of 5 wt%  $\text{SnO}_2$  and 95 wt%  $\text{In}_2\text{O}_3$ . Initially, the chamber pressure was pumped down to  $5 \times 10^{-6}$  Torr. During the evaporation, nitrogen gas with a flow rate of 1 sccm flow was introduced into the chamber and maintained at a pressure of  $1 \times 10^{-4}$  Torr. Nitrogen flow is essential for maintaining the chamber in a deoxygenated environment. Short and long ITO NRs were deposited at an angle of  $70^\circ$ . The deposition temperature was  $200^\circ\text{C}$ , and the deposition rate was kept at  $1.5 \text{ \AA/s}$ . The deposition time for the short and long ITO NRs were 13 and 22 minutes, respectively. On the other hand, short and long ITO NWs were deposited at the angles of  $50^\circ$  and  $70^\circ$ , respectively. The deposition times were 22 and

26 minutes, respectively. Besides, the deposition temperatures were 210°C and 190°C, respectively. The growth conditions of ITO nanomaterials are summarized in Table 1. Figure 1 shows the scanning electron microscopy (SEM) images of the ITO NRs and NWs. The tilted top views of short and long NRs, short and long NWs are shown in Figs. 1(a) and 1(c), Figs. 1(e) and 1(g), respectively. The corresponding cross-sectional images of these nanomaterials are shown in Figs. 1(b) and 1(d), Figs. 1(f) and 1(h), respectively. The heights of ITO NRs are estimated to be 621.1 nm and 991.6 nm, while those of the NWs are 802.6 nm and 1169.5 nm, respectively. All samples are deposited on double-side-polished silicon wafer with high resistivity. Here, samples of NRs and NWs all exhibit high-density and uniform morphology. This is different from the samples in our previous study [27]. Therefore, the volume filling factors ( $f$ ) of ITO nanomaterials in this study can be defined accurately from the SEM figures.

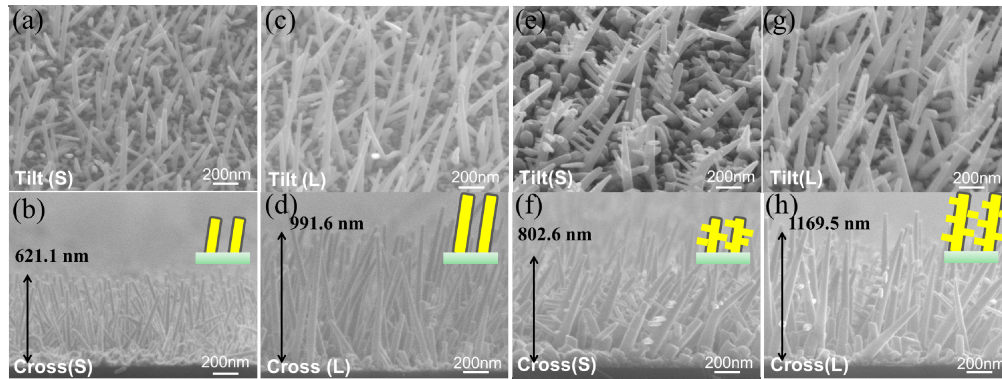


Fig. 1. The scanning electron microscopy (SEM) images of the ITO nanomaterials fabricated by the electron-beam GLAD system: (a) short NRs, (c) long NRs, (e) short NWs, and (g) long NWs. The corresponding cross-sectional SEM images of these samples are shown in (b), (d), (f) and (h). Cartoons of the nanomaterials and their estimated heights are also indicated.

**Table 1. Deposition conditions for ITO nanomaterials by the electron-beam GLAD system**

	<i>NRS (621.1 NM)</i>	<i>NRS (991.6 NM)</i>	<i>NWHS (802.6 NM)</i>	<i>NWHS (1169.5 NM)</i>
<b>DEPOSITION ANGLE</b>	70°	70°	50°	70°
<b>DEPOSITION TEMP.</b>	200°C	200°C	210°C	190°C
<b>DEPOSITION TIME</b>	13 MIN.	22 MIN.	22 MIN.	26 MIN.

## 2.2. THz-TDS systems

For extraction of complex optical constants of the nanomaterials, we employed two THz time-domain spectrometers (THz-TDS). Both systems are purged with dry nitrogen so that they can be maintained at a relative humidity of  $4.0 \pm 0.5\%$ . One system is based on broadband THz emission from laser-induced gaseous plasma. The experimental setup is shown schematically in Fig. 2(a). For excitation, the fundamental beam ( $\omega$ ) comes from a Ti:Sapphire amplifier (Spitfire, Spectra Physics) which generates 70-fs pulses at a repetition rate of 1 kHz. The central wavelength was 815 nm. Second harmonic pulses ( $2\omega$ ) were generated from the fundamental from a 100- $\mu\text{m}$ -thick  $\beta$  barium-borate (BBO) crystal cut for type-I phase-matching. Both the fundamental and second-harmonic pulses were focused into nitrogen with a 150mm-focal length convex lens to generate the plasma filament. The polarized THz radiation from the plasma filament was then collimated and refocused onto the sample. A two-side-polished high-resistivity silicon wafer was inserted to block the optical beams after the plasma filament. For detection of the THz waveform, we used electro-optical (EO) sampling [38] with a 300- $\mu\text{m}$ -thick gallium phosphide (GaP) crystal. The dynamic range

of the laser-induced air plasma THz-TDS was as high as  $10^6$  over the frequency range of 0.45~9.00 THz. An antenna-based THz-TDS, as described in our previous works [17, 27, 39, 40], was employed for complementary measurements with similar dynamic ranges over the frequency range of 0.15~3.00 THz. The spectroscopic characteristics of the latter system are also shown in Fig. 2. Employing both systems, we can get reliable measurements in the frequency range of 0.15~9.00 THz.

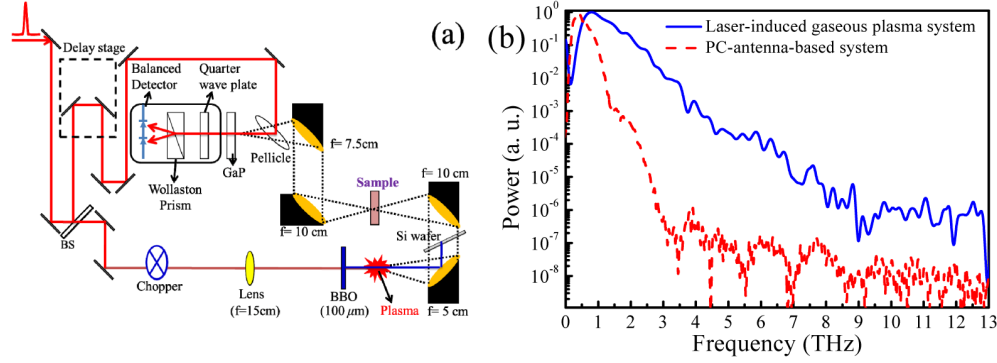


Fig. 2. (a) Schematic of the experimental setup for the THz-TDS based on laser-induced gaseous plasma. The THz field is generated by dual-color (800-nm and 400-nm) femtosecond pulses from an amplified Ti:Sapphire laser in the gaseous plasma. Terahertz pulses are detected with EO sampling with a GaP crystal. (b) Typical performance of the THz-TDS systems based on laser-induced gaseous plasma (blue solid line), and PC antenna (red dash line), respectively, are shown.

### 2.3. Extraction of optical parameters and complex conductivities with Drude-Smith model approach

Previously, we performed THz-TDS studies of ITO NWs by treating the nanomaterial, which was low-density and did not cover uniformly on the substrate, as a graded-refractive-index (GRIN) structure [27]. This is confirmed by depth-resolved ellipsometric measurements in the visible. In this study, the ITO NRs and NWs have denser and much more uniform morphologies than the previous work. Besides, we are interested in effective optical and electrical properties of nanomaterials for applications in THz devices. Therefore, the samples are treated as thin films in the effective medium approximation (EMA).

The method we employed for extraction of optical parameters of the nanomaterials has been described previously [17, 33]. Specifically, the complex transmission coefficient of nanomaterials (or thin films) is described as

$$T_{\text{Sam}}^*(\omega) = \frac{E_{\text{Sam}}^*(\omega)}{E_{\text{Ref}}^*(\omega)} = \frac{t_{12}^* t_{23}^* \exp[i \cdot (n_2^* - 1) \cdot d \cdot \omega / c]}{t_{13}^* \cdot [1 - r_{21}^* r_{23}^* \exp(i \cdot 2n_2^* \cdot d \cdot \omega / c)] \cdot \exp[i \cdot (n_3^* - 1) \cdot \Delta d \cdot \omega / c]} \quad (1)$$

Here,  $E_{\text{Sam}}^*(\omega)$  and  $E_{\text{Ref}}^*(\omega)$  are electric fields of the THz wave transmitted through the nanomaterials (or thin films) and the bare substrate, respectively. The parameters,  $t_{12}^*$ ,  $t_{23}^*$  and  $t_{13}^*$  are the transmission coefficients of the THz signal from air to the nanomaterials (or thin films), from nanomaterials (or thin films) to the substrate, and from air to the substrate, respectively. Similarly,  $r_{23}^*$  and  $r_{21}^*$  are the reflection coefficients of the THz signal from the nanomaterials (or thin films) to the substrate, and from nanomaterials (or thin films) to air, respectively. Here,  $n_2^*$  and  $n_3^*$  are the equivalent refractive indices of the nanomaterials (or thin films) and the substrate, respectively. Additionally,  $d$  is thickness of the nanomaterials (or thin films);  $\omega$  and  $c$  are the angular frequency and speed of light in vacuum, respectively.

Further, the slight difference of the thickness between the sample and reference substrates is taken into account by  $\Delta d$ . After numerically solving Eq. (1), one can extract the refractive indices  $n$  and  $\kappa$  ( $n_2^* = n + i\kappa$ ) of the nanomaterials (or thin films) under investigation.

ITO nanomaterials are viewed as a composite of ITO and air. In the EMA, their effective dielectric constant can be written as,  $\epsilon_{\text{effective}}^* = f \times \epsilon_m^* + (1-f) \times \epsilon_h^*$  [17, 33]. Here,  $f$  is the filling factor which defines the volume fraction of the nanomaterials. The parameters  $\epsilon_h^*$  and  $\epsilon_m^*$  are the dielectric function of air (host medium) and pure nanomaterials, respectively. In this approximation, the real ( $\text{Re}\{\sigma\}$ ) and imaginary ( $\text{Im}\{\sigma\}$ ) parts of pure ITO nanomaterials can be derived from the measured optical constants as  $\text{Re}\{\sigma\} = \omega \epsilon_0 \cdot (2n\kappa) / f$  and  $\text{Im}\{\sigma\} = \omega \epsilon_0 [\epsilon_\infty - [n^2 - \kappa^2 - (1-f)] / f]$ , respectively. Here,  $\epsilon_\infty = 4$  [17, 27, 28], is the high-frequency dielectric constant;  $\epsilon_0 = 8.854 \times 10^{-12}$  (F/m) is the free-space permittivity.

In order to describe the material system with long-range transport which is suppressed by disorder, the Drude-Smith model, an extension of the Drude model proposed by N. V. Smith [42], is applied to fit the experimental results. The complex conductivity of the nanomaterial can be written as

$$\sigma^*(\omega) = \frac{\epsilon_0 \omega_p^2 \tau}{1 - i\omega\tau} \left( 1 + \frac{\gamma}{1 - i\omega\tau} \right). \quad (2)$$

Here,  $\omega_p$  and  $\tau$  are the plasma frequency and the carrier scattering time, respectively. The parameter  $\gamma$  is the carrier's persistence of velocity after experiencing one collision, in other words, it is associated with the degree of carrier localization. The value of  $\gamma$  can vary from 0 to  $-1$ , corresponding to the limit of isotropic scattering to full carrier localization. The Drude-Smith model has been a common choice for describing the complex conductivities of nanostructured materials, e. g., ITO NWs, TiO<sub>2</sub> nanomaterials, ZnO nanomaterials, and SnO<sub>2</sub> nanowires in the THz frequency range [17, 27, 29–34, 43].

### 3. Results and discussions

For the frequency range below 0.50 THz and above 1.40 THz, we used data taken from the PC antenna and laser-induced gaseous plasma based systems, respectively. Between 0.50 and 1.40 THz, the data from the two systems were identical within experimental error. In order to discuss the effect of morphology on electrical properties of the nanomaterials, the volume filling factors,  $f$ , of ITO short NRs, long NRs, short and long NWs were estimated to be 17.9%, 9.8%, 20.0%, and 10.3% by examining Fig. 1.

The frequency-dependent transmittance of ITO NRs, NWs and thin films, shown in the Fig. 3 are plotted in the THz frequency range 0.20~15.00 THz. In addition to THz-TDS measurement, we have also conducted Fourier transform infrared spectroscopic (FTIR) using a (Bruker, Vertex 70V) from 0.50 to ~15.00 THz. Combining the results of both type of experiments, we find that the transmittance of shorter and longer NRs are around 65% and 73%. On the other hand, the transmittances of short and long NWs are ~19% and ~65%, respectively. In general, by increasing the height of ITO nanomaterials, one can substantially increase their transmittance. Significantly, ITO NWs exhibited conspicuous morphology-dependent transmittance. Plausibly, the longitudinal change of refractive indices of shorter NWs is stronger than that of the longer one. As a result, the AR function of shorter ITO NWs is not so apparent. For comparison, the transmittance of sputtered ITO thin films with thicknesses of 345.0 nm and 1062.0 nm in the same frequency range are much smaller, 9% and 4%. These are also plotted in Fig. 3 for comparison. Clearly, because of the broadband GRIN characteristic, the morphologies of NRs and long NWs have outstanding transmission of electric field in the THz and far-infrared frequency range.

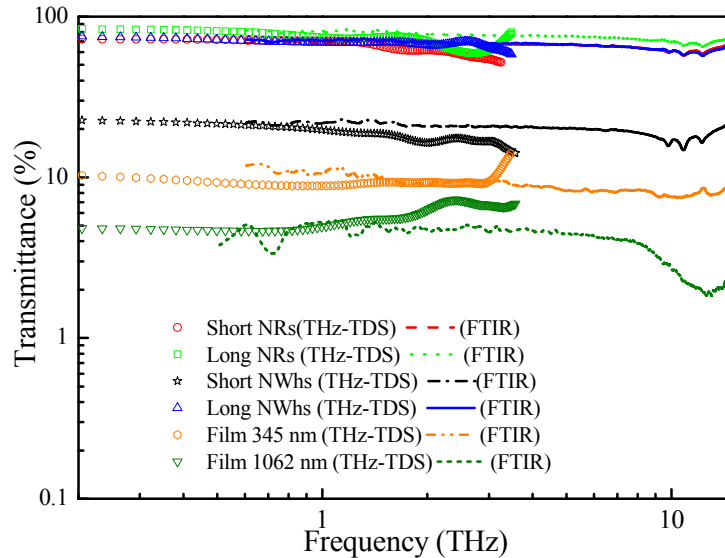


Fig. 3. The transmittance of ITO nanomaterials and thin films are plotted as a function of frequency. The red circles, green squares, black stars, blue triangles, orange hexagon, and olive inverted triangles are experimental data from THz-TDS measurements. The red-dash, green-dot, black-dash dot, blue-solid, orange-dash dot, and olive-short dash curves are experimental data from FTIR measurements.

The frequency-dependent refractive indices ( $n$ ), and extinction coefficients ( $\kappa$ ) for ITO NRs and NWs with air composite, together with sputtered ITO thin films of difference thickness are shown in Fig. 4. In the frequency range of 0.20~4.00 THz, the equivalent refractive indices of the air composite of short NRs, long NRs, and long NWs are not far apart, around 6.18, 4.96, and 4.26, respectively. However, the equivalent  $n$  of short NWs decreases monotonically from 23.83 to 3.77 in this frequency, with a root-mean-square value of  $\sim 11.51$ . For the same type of nanomaterial (NRs or NWs), the equivalent  $n$  of longer NRs ( $4.85 < 5.86$ ) and NWs ( $3.87 < 11.23$ ) is much more close to that of the air, partially explaining the superior transmission properties of longer ITO NRs and NWs. The refractive indices ( $n$ ) of ITO thin film with thicknesses of 345 nm and 1062 nm are plotted in Fig. 4(a). These samples show a dramatic decreasing trend in  $n$  from 52.07 to 11.74, and from 38.98 to 14.75 in the 0.20~4.00 THz frequency range, respectively. The extinction coefficients ( $\kappa$ ) of ITO NRs and NWs with air composite, together with sputtered ITO thin films of difference thickness are shown in the Fig. 4(b). These exhibits almost the same trend of  $n$ . Previously, C. A. Schmuttenmaer et al., and G. Ma et al. have characterized the optical constants of ZnO nanomaterials [31], and its sputtered thin film [32]. ZnO thin films exhibit a relatively steep drop in refractive index, from 90 to 30, in the frequency range 0.1~1.0 THz, which resembles the trend for ITO thin films. On the other hand, ZnO nanomaterials show relatively less fluctuating values of optical constants. In general, complex optical constants of ITO NWs, and thin films reported in this work are in agreement of our previous studies of the same material system, which provides data below 2 THz [17, 28]. Besides, we have also studied the bottom thin film layer of ITO NWs atop the substrate. This layer is characterized by values of  $n$  that decrease monotonically from 68 to 40, and increasing values of  $\kappa$  from 10 to 30 in the range of 0.2~2.0 THz [27]. Using the data in Fig. 4, the penetration depths ( $\delta_p$ ) of short NRs, long NRs, short NWs, thinner (345 nm) and thicker (1062 nm) ITO films at 2.00 THz, are estimated to be 2.29  $\mu\text{m}$ , 5.26  $\mu\text{m}$ , 1.26  $\mu\text{m}$ , 2.90  $\mu\text{m}$ , 0.77  $\mu\text{m}$ , and 0.86  $\mu\text{m}$ , respectively. Here, the taller samples of each class of ITO nanomaterials have larger values of  $\delta_p$ , while long NRs (991.6 nm) exhibits lower absorption than comparable NWs (802.6 and 1169.5



nm) with the nearly the same height in the frequency range 0.2~4.0 THz. To compare,  $\delta_p$  of ITO thin films is always lower than 0.90  $\mu\text{m}$ .

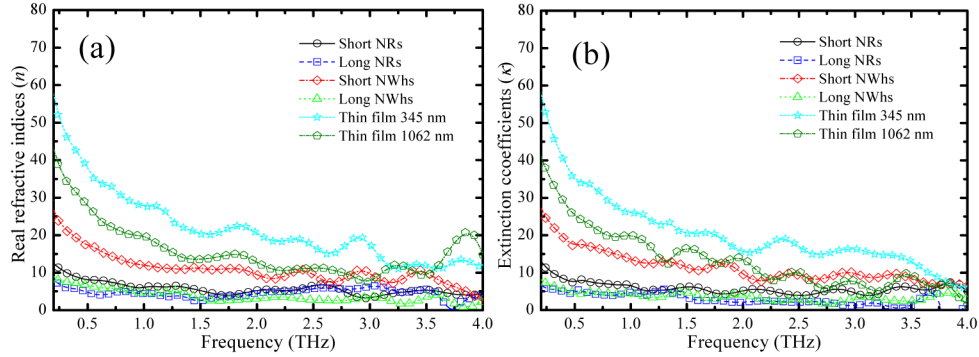


Fig. 4. (a) Real refractive indices, (b) extinction coefficients of ITO nanomaterials and thin films are plotted as a function of frequency. The black-solid line with circles, blue-dash line with squares, red-dash dot line with diamonds, green-dot line with triangles, cyan-short dash line with stars, and olive-short dash dot line with pentagons correspond to the optical constants for short NRs, long NRs, short NWs, long NWs, thin film 345 nm, and thin film 1062 nm.

The complex conductivities of ITO nanomaterials with different heights and morphologies, are shown in Figs. 5(a) and 5(b), respectively. The real conductivities or  $\text{Re}\{\sigma\}$  of both types of nanomaterials are suppressed at lower frequencies. Meanwhile, negative values of  $\text{Im}\{\sigma\}$  are observed. Such phenomena are typically associated with carrier localization in the materials [17, 27, 29, 30, 33, 34, 43]. Based on these observations, the Drude-Smith model, rather than the Drude model, should be applied to fit the experimentally extracted complex conductivity [42]. As shown in Figs. 5(a) and 5(b),  $\text{Re}\{\sigma\}$  and  $\text{Im}\{\sigma\}$  of ITO materials can be fit excellently this way. All of the fitting parameters are summarized in Table 2. Regarding NRs with heights of 621.1 and 991.6 nm, the plasma frequencies are 561 versus 1006  $\text{rad}\cdot\text{THz}$ ; carrier scattering times are 31.7 versus 13.5 fs; the parameters  $\gamma$  are  $-0.71$  versus  $-0.88$ . For the NWs with heights of 802.6 and 1169.5 nm, the plasma frequencies are 751 versus 853  $\text{rad}\cdot\text{THz}$ ; carrier scattering times are 39.6 versus 13.2 fs; the parameters  $\gamma$  are  $-0.60$  versus  $-0.74$ . All  $\gamma$  values of the nanomaterials are smaller than  $-0.50$  (approaching  $-1.00$ ). Such behavior indicates the presence of significant carrier localization effects in ITO NRs and NWs.

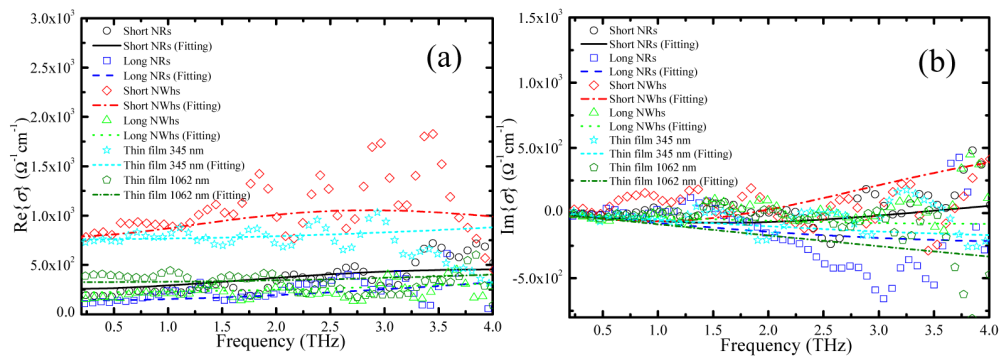


Fig. 5. (a)  $\text{Re}\{\sigma\}$ , (b)  $\text{Im}\{\sigma\}$  of ITO nanomaterials and thin films are plotted as a function of frequency. The black circles, blue squares, red diamonds, green triangles, cyan stars, and olive pentagons are experimental data. The black-solid line, blue-dash line, red-dash dot line, green-dot line, cyan-short dash line, and olive-short dash dot line are fitting curves based on the Drude-Smith model.

In our previous study, we have identified the mechanism of carrier localization in ITO NWs to be the carrier scattering from grain boundaries and impurity ions (Tin) [17]. At room temperature (~300K), the mean free paths of ITO NRs and NWs are estimated to be in the range of 2.88~6.76 nm and 2.81~8.44 nm, respectively. For these two classes of nanomaterials, their carrier mean free paths are thus pretty close. X-ray diffraction (XRD) studies indicated that ITO NWs are polycrystalline and the size of (222) preferred orientation of nanograins is around 18 nm [17]. Because the grain size and mean free path are both of the nano-scale, the carrier scattering caused by the grain boundary in ITO nanomaterials is significant. Furthermore, from the relations  $N_e = \epsilon_0 \omega_p^2 m^* / e^2$ ,  $\mu = (1 + \gamma) e \tau / m^*$ , and  $\sigma_0 = \epsilon_0 \omega_p^2 \tau (1 + \gamma)$ , the parameters,  $N_e$ ,  $\mu$  and  $\sigma_0$  of ITO nanomaterials can be determined. Here, we take  $m^* = 0.3m_0$  to be the electron effective mass [17, 27]; where  $m_0 = 9.1094 \times 10^{-31}$  kg, is the electron's mass;  $e = 1.602 \times 10^{-19}$  C, is the electron charge. For ITO NRs with different heights, 621.1 and 991.6 nm, the corresponding  $N_e$ ,  $\mu$  and  $\sigma_0$  are determined to be 2.97 versus  $9.56 \times 10^{19}$  cm<sup>-3</sup>, 53.6 versus 9.1 cm<sup>2</sup>V<sup>-1</sup>s<sup>-1</sup> and 255.3 versus 145.2  $\Omega^{-1}$ cm<sup>-1</sup>, respectively. In comparison, for ITO NWs with heights of 802.6 and 1169.5 nm, the corresponding  $N_e$ ,  $\mu$  and  $\sigma_0$  of are 5.33 versus  $6.86 \times 10^{19}$  cm<sup>-3</sup>, 92.0 versus 20.3 cm<sup>2</sup>V<sup>-1</sup>s<sup>-1</sup> and 791.0 versus 221.1  $\Omega^{-1}$ cm<sup>-1</sup>, respectively. All of these electrical properties of the ITO nanomaterials are summarized in Table 2. Previously, the effect of carrier localization can be enhanced by the charged impurity (Tin) scattering centers in ITO [17, 44]. From the carrier concentration we calculated, the average distance between dopant ions for ITO NRs and NWs, which is proportional to the inverse of the third root of doping concentration, is 2.19~3.23 nm and 2.44~2.66 nm, respectively. Recalling the  $L_{\text{free}}$  of ITO NRs (2.88~6.76 nm) and NWs (2.81~8.44 nm), the free carriers will run into the scattering center more than once. In other words, carrier localization in both ITO nanomaterials can also be attributed to scattering of the carriers with impurity ions. Taking into account of their nearly identical volume filling factors, the mobilities of short and long NWs (92.0 and 20.3 cm<sup>2</sup>V<sup>-1</sup>s<sup>-1</sup>) are much larger than those NRs (53.6 and 9.1 cm<sup>2</sup>V<sup>-1</sup>s<sup>-1</sup>) due to slight difference in carrier localization effects between the two class of nanomaterials. This behavior can be attributed to that the direction of branches of ITO nanowhiskers is parallel to the THz radiation, so that it strengthens the ability of transporting the electrons. We note that other functional TCOs, e.g., tin oxide (SnO<sub>2</sub>) NWs, nanocrystalline TiO<sub>2</sub> and ZnO NWs, and all exhibit the characteristic of carrier localization. Their  $\gamma$  parameters or the carrier's persistence of velocity after experiencing one collision are respectively ( $\gamma \cong -0.92 \sim -1$ ) [33, 34], ( $\gamma \cong -0.93$ ) [29] and ( $\gamma \cong -0.92$ ) [31]. In comparison, the  $\gamma$  parameters for ITO NRs and NWs are somewhat smaller, i.e., ( $\gamma \cong -0.71 \sim -0.88$ ) and ( $\gamma \cong -0.60 \sim -0.74$ ), respectively. That is, the effect of carrier localization in ITO nanomaterials is not so severe. This is consistent with the relatively lower mobilities of SnO<sub>2</sub> NWs, TiO<sub>2</sub> nanocrystalline, and ZnO NWs are 20~72 cm<sup>2</sup>V<sup>-1</sup>s<sup>-1</sup>, 1.5 cm<sup>2</sup>V<sup>-1</sup>s<sup>-1</sup>, and ~16 cm<sup>2</sup>V<sup>-1</sup>s<sup>-1</sup>, respectively [29, 31, 33, 34], as compared to those of ITO nanomaterials.

In Figs. 5(a) and 5(b), we have also plotted the  $\text{Re}\{\sigma\}$  and  $\text{Im}\{\sigma\}$  of ITO thin films with thickness of 345 nm and 1062 nm. All of the fitting parameters for the dielectric and electrical properties of ITO thin films are also summarized in Table 2. Regarding, For example, the  $N_e$ , and  $\mu$  of the aforementioned ITO thin films are determined to be 29.3 versus  $94.9 \times 10^{19}$  cm<sup>-3</sup>, and 16.2 versus 2.1 cm<sup>2</sup>V<sup>-1</sup>s<sup>-1</sup>, respectively. Clearly,  $\mu$ 's of ITO thin films are poorer than those of ITO nanomaterials because the higher concentration of dopant ions in ITO thin films due to the strong carrier scattering effects. This behavior has not been uncovered in our previous study [17]. It is now our understanding that the fitting spectral range in describing the non-Drude behavior must be broad enough. Besides, the sputtered ITO thin film is amorphous [17]. Meanwhile, the  $L_{\text{free}}$  of ITO thin films and the average distance between dopant ions are 0.92~1.92 nm and 1.02~1.51 nm, respectively. Therefore, carrier localization in ITO thin films is dominated by scattering with impurity ions.

**Table 2. Extracted parameters of ITO nanomaterials and thin films based on the Drude-Smith Model**

<i>Samples</i>	$\omega_p$ (rad·THz)	$\tau$ (fs)	$\gamma$	$N_e$ ( $\times 10^{19}$ cm <sup>-3</sup> )	$\mu$ (cm <sup>2</sup> V <sup>-1</sup> s <sup>-1</sup> )	$\sigma_0$ ( $\Omega^{-1}$ cm <sup>-1</sup> )
Short NRs	561	31.7	-0.71	2.97	53.6	255.3
Long NRs	1006	13.5	-0.88	9.56	9.1	145.2
Short NWs	751	39.6	-0.60	5.33	92.0	791.0
Long NWs	853	13.2	-0.74	6.86	20.3	221.1
Thin film (345 nm)	1761	9.0	-0.69	29.3	16.2	765.2
Thin film (1062 nm)	3170	4.3	-0.92	94.9	2.1	307.5

In Fig. 6, the complex conductivities fitted in different frequency ranges measured by the PC-antenna-based THz-TDS system only (0.2~1.4 THz, yellow region) and by both THz-TDS systems (0.2~4.0 THz) are shown. Note that the trends of fits of complex conductivities for the two data sets are consistent in the THz frequency range in which the two overlapped, i.e., 0.2~1.4 THz. There are also apparent minimum and maximum values of the real and imaginary parts of conductivities for the samples investigated. The angular frequencies for the maximum value of  $\text{Re}\{\sigma\}$ , maximum value of  $\text{Im}\{\sigma\}$ , minimum of  $\text{Im}\{\sigma\}$ , and crossing of  $\text{Im}\{\sigma\}$  and the frequency axis, which are given by  $\omega_{\text{Re,Max}} = [-(1 + 3\gamma)/(1-\gamma)]^{1/2}/\tau$ ,  $\omega_{\text{Im,Max}} = [-3\gamma + (9\gamma^2 + 2\gamma + 1)^{1/2}]^{1/2}/\tau$ ,  $\omega_{\text{Im,Min}} = [-3\gamma - (9\gamma^2 + 2\gamma + 1)^{1/2}]^{1/2}/\tau$ , and  $\omega_{\text{Im,Zero}} = (-1-2\gamma)^{1/2}/\tau$ , respectively [17, 27]. Their positions are indicated by arrows in Fig. 6. These characteristic frequencies for ITO NRs, NWs and sputtered thin films, accordingly to the Drude-Smith model, are also summarized in Table 3. Clearly, these extreme values of  $\text{Re}\{\sigma\}$  and  $\text{Im}\{\sigma\}$  as well as the inflection points are functions of the carrier scattering time ( $\tau$ ) and the expectation value of cosine of the scattering angle ( $\gamma$ ). If  $\omega_{\text{Re,Max}}/2\pi$ ,  $\omega_{\text{Im,Min}}/2\pi$ , etc., are located above 1.40 THz or the estimated limit of extraction of reliable dielectric and electrical parameters of nanomaterials for our PC-antenna-based system, the values of parameters such as  $\tau$  and  $\gamma$  could be questionable. For example,  $\omega_{\text{Re,Max}}/2\pi$ , and  $\omega_{\text{Im,Min}}/2\pi$ , of short ITO NRs shown in Fig. 6(a), are 4.09 THz, and 1.60 THz, respectively. Both of them are larger than 1.40 THz. The extreme values of the fitting curves for conductivities based on this narrower-band data set shift to higher frequencies, as opposed to the results from data set for 0.2~4.0 THz. The phenomena of shifting of extreme values of complex conductivities for other ITO samples can also be found in Figs. 6(b)-6(f). Clearly, consideration of the extreme values provide a possibly additional criteria for assessing the accuracy of the extraction of electrical parameters of non-Drude-like materials using THz-TDS. We note that quite a few works that applied Drude-Smith model to fit the complex conductivity are based on data taken below 2.5 THz [17, 29, 31, 33, 43].

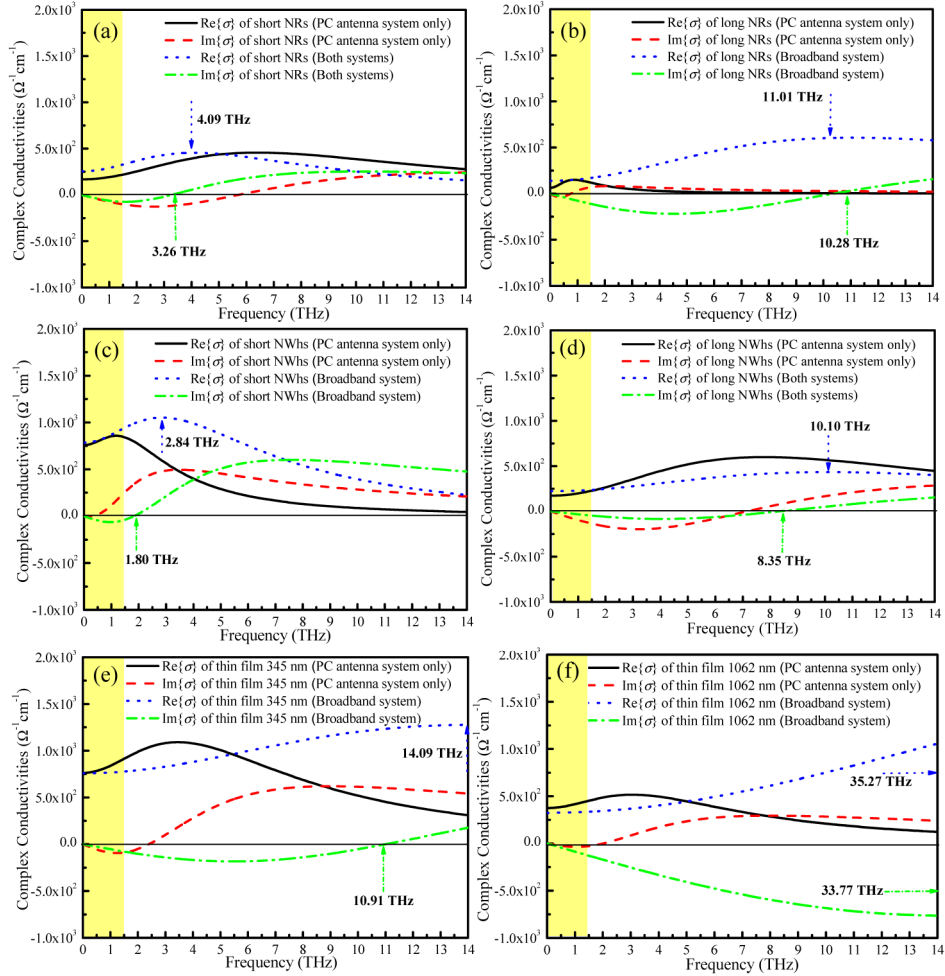


Fig. 6. Fitting curves of THz complex conductivities of (a) short NRs, (b) long NRs, (c) short NWs, (d) long NWs, (e) 345-nm-thick sputtered film, and (f) 1062-nm-thick sputtered film using experimental data from the PC-antenna-based system only (0.15~1.4 THz, yellow region), and 0.15~4.0 THz (both THz-TDS systems). The black solid line, red dash line, blue dot line, and green dash dot line are fitting curves of  $\text{Re}\{\sigma\}$  as measured by the PC-antenna-based system only,  $\text{Im}\{\sigma\}$  as measured by the PC-antenna-based system only,  $\text{Re}\{\sigma\}$  as measured by both THz-TDS systems, and  $\text{Im}\{\sigma\}$  as measured by both THz-TDS, respectively.

Even though Drude-Smith model was applied successfully to describe the experimental data, the trend of THz complex conductivities seems also conform to the model of free-electron plasma with a plasmon resonance. This is implied by nearly the same values of  $\omega_{\text{Re, Max}}/2\pi$ , and  $\omega_{\text{Im, Zero}}/2\pi$  for each sample (see Table 3). The plasmon-like model, as discussed by V. Sundström et al. [45], determines the plasmon frequency of the material from the values of  $\omega_{\text{Re, Max}}/2\pi$ , and  $\omega_{\text{Im, Zero}}/2\pi$ . In 2007, P. Parkinson et al. applied the plasmon-like model to describe complex conductivities of GaAs nanowires [46]. In their study, a redshift of the plasmon frequency with decreasing the charge carrier density was also observed [46]. In the present work, the decrease in carrier density corresponding to reducing heights of ITO nanomaterials and thin films is reflected by a redshift of  $\omega_{\text{Re, Max}}/2\pi$ , and  $\omega_{\text{Im, Zero}}/2\pi$ , respectively. For instance,  $\omega_{\text{Re, Max}}/2\pi$  of NRs shifts from 11.01 THz to 4.09 THz as the height decreases from 991.6 nm to 621.1 nm, while  $\omega_{\text{Im, Zero}}/2\pi$  also decreases from 10.28 THz to

3.26 THz. This behavior is indicated by the blue-dot and green dash-dot arrows Figs. 6(a)-6(f), respectively.

**Table 3. Characteristic values of complex conductivities of ITO nanomaterials and thin films measured by broadband THz-TDS**

Samples	$\omega_{\text{RE,MAX}}/2\pi$ (THz)	$\omega_{\text{IM,MAX}}/2\pi$ (THz)	$\omega_{\text{IM,MIN}}/2\pi$ (THz)	$\omega_{\text{IM,ZERO}}/2\pi$ (THz)
Short NRs	4.09	10.25	1.60	3.26
Long NRs	11.01	26.71	4.54	10.28
Short NWs	2.84	7.57	0.95	1.80
Long NWs	10.10	25.09	4.01	8.35
Thin film (345 nm)	14.09	35.61	5.43	10.91
Thin film (1062 nm)	35.27	85.32	14.58	33.77

#### 4. Conclusions

Indium-tin-oxide (ITO) nanorods (NRs) and nanowhiskers (NWs) were fabricated by an electron-beam glancing-angle deposition GLAD system. Two terahertz (THz) time-domain spectrometers (TDS), based respectively on dual-color laser-induced gaseous plasma and photoconductive antenna, were applied to study the optical and electrical properties of such ITO nanomaterials in the frequency range from 0.20 to 4.00 THz. Together with Fourier transform infrared spectroscopic (FTIR) measurements, we found that both the THz and far-infrared transmittance of these nanomaterials can be as high as 70% as opposed to about 9% for sputtered ITO thin films. The complex conductivities of ITO NRs, NWs as well as films are well fitted by the Drude-Smith model. Taking into account that the volume filling factors of both type of nanomaterials are nearly same, mobilities of short and long ITO NWs (92.0 and 20.3  $\text{cm}^2\text{V}^{-1}\text{s}^{-1}$ ) are higher than those of NRs (53.6 and 9.1  $\text{cm}^2\text{V}^{-1}\text{s}^{-1}$ ) of nearly the same heights due to less severe carrier localization effects in the former. On the other hand, mobilities of sputtered ITO thin films are poorer than ITO nanomaterials because of larger (~10 times) concentration of dopant ions in films, which causes stronger carrier scattering. We note further that consideration of the extreme values of  $\text{Re}\{\sigma\}$  and  $\text{Im}\{\sigma\}$  as well as the inflection points, which are functions of the carrier scattering time ( $\tau$ ) and the expectation value of cosine of the scattering angle ( $\gamma$ ), provide additional criteria for assessing the accuracy of the extraction of electrical parameters of non-Drude-like materials using THz-TDS. Our studies so far indicate ITO NWs with heights of ~1000 nm show outstanding transmittance and good electrical characteristics for applications such as transparent conducting electrodes of THz Devices.

#### Acknowledgments

This work was funded by the grant of the National Science Council 101-2221-E-007-103-MY3 and the Academic Top University Program of the Ministry of Education. The authors would like to thank Professor Hao-Chung Kuo in National Chiao Tung University for the use of the electron-beam GLAD system. They would also like to thank Dr. Jia-Min Shieh for providing the ITO thin films. Finally, they would like to thank Professor Ta-Jen Yen for use of the FTIR spectrometer.